catalysts

MDPI

Article

Fabrication of FeTCPP@CNNS for Efficient Photocatalytic Performance of p-Nitrophenol under Visible Light

Shiyun Li [1,†], Yuqiong Guo [1,†], Lina Liu [1], Jiangang Wang [1], Luxi Zhang [1], Weilong Shi [1,*], Malgorzata Aleksandrzak [2], Xuecheng Chen [2,*] and Jie Liu [3]

[1] School of Materials Science and Engineering, Jiangsu University of Science and Technology, Zhenjiang 212003, China
[2] Faculty of Chemical Technology and Engineering, West Pomeranian University of Technology, Piastów Ave. 42, 71-065 Szczecin, Poland
[3] State Key Laboratory of Polymer Physics and Chemistry, Changchun Institute of Applied Chemistry, Chinese Academy of Sciences, Changchun 130022, China; liujie@ciac.ac.cn
* Correspondence: shiwl@just.edu.cn (W.S.); xchen@zut.edu.pl (X.C.)
† These authors contributed equally to this work.

Abstract: A photocatalyst of iron–porphyrin tetra-carboxylate (FeTCPP)-sensitized g-C_3N_4 nanosheet composites (FeTCPP@CNNS) based on g-C_3N_4 nanosheet (CNNS) and FeTCPP have been fabricated by in situ hydrothermal self-assembly. FeTCPP is uniformly introduced to the surface of CNNS. Only a small amount of FeTCPP is introduced, and the stacked lamellar structure is displayed in the composite. As compared with pure CNNS, the FeTCPP@CNNS composites exhibit significantly improved photocatalytic performance by the photodegradation of p-nitrophenol (4-NP). At the optimum content of FeTCPP to CNNS (3 wt%), the photodegradation activity of the FeTCPP@CNNS photocatalyst can reach 92.4% within 1 h. The degradation rate constant for the 3% FeTCPP@CNNS composite is 0.037 min^{-1} (4-NP), which is five times that of CNNS (0.0064 min^{-1}). The results of recycling experiments show that 3% FeTCPP@CNNS photocatalyst has excellent photocatalytic stability. A possible photocatalytic reaction mechanism of FeTCPP@CNNS composite for photocatalytic degradation of 4-NP has been proposed. It is shown that superoxide radical anions played the major part in the degradation of 4-NP. The appropriate content of FeTCPP can enhance the charge transfer efficiency. The FeTCPP@CNNS composites can provide more active sites and accelerate the transport and separation efficiency of photogenerated carriers, thus further enhancing the photocatalytic performance.

Keywords: FeTCPP@CNNS; g-C_3N_4 nanosheets; photocatalytic; visible light

Citation: Li, S.; Guo, Y.; Liu, L.; Wang, J.; Zhang, L.; Shi, W.; Aleksandrzak, M.; Chen, X.; Liu, J. Fabrication of FeTCPP@CNNS for Efficient Photocatalytic Performance of p-Nitrophenol under Visible Light. *Catalysts* **2023**, *13*, 732. https://doi.org/10.3390/catal13040732

Academic Editor: Weilin Dai

Received: 9 March 2023
Revised: 6 April 2023
Accepted: 10 April 2023
Published: 12 April 2023

1. Introduction

With the fast development of economy and industry, environmental deterioration—especially water pollution by organic dyes, which result in a serious threat to human health—has garnered wide attention from the government and society. At present, many effective methods have been used to resolve water pollutant problems, including the membrane oxidation method, adsorption method, separation method, and photocatalysis method [1–4]. Photocatalysis are proved to be a safe, economical, and renewable method to solve the aforementioned pollution problems by photocatalysts at ambient pressure and room temperature under solar light, which is considered one of the most promising wastewater treatment methods [5]. Although the application of photocatalytic technology has been wildly used, there is still a puzzle to develop photocatalysts with physicochemical stability, photocatalytic activity, and enhancing visible light utilization efficiency for practice application [6]. Photocatalytic reaction can be divided into three basic processes, including light capture process, carrier separation and migration process, and photocatalytic redox reaction [7–12].

Metal-free polymeric semiconductor graphite-like carbon nitride (g-C_3N_4), with a large amount of of pendant amine and unique two-dimensional structure, is a promising candidate for solar energy conversion and organic pollutions degradation by solar irradiation due to its easy fabrication, good chemical and physical stability, nontoxicity, low cost, and visible light activity. The g-C_3N_4 possesses a bandgap of approx. 2.7 eV, which has presented good chemical stability in the removal of organic dyes and high visible light absorption ability. However, the photocatalytic activity and the practical application of g-C_3N_4 are restricted by the fast recombination of the photogenerated electron–hole carriers [13]. To break these limitations, many studies have been adopted to depress the rapid recombination of carriers, such as the morphology control of g-C_3N_4, doping, combination with other semiconductors, surface sensitization, and dye sensitization [14,15].

As one of the light-harvesting materials, porphyrins play an important role in photocatalysis. Porphyrin compounds act as excellent photosensitizers for photocatalysts due to their wide absorption band, large conjugate structure, and good electron-donating properties [14,16,17]. In general, under UV and visible light irradiation, metalloporphyrins can catalyze a great many oxidative transformations. The metalloporphyrins can be combined with photocatalysts in the outer of the porphyrin ring through covalent interaction among the different functional groups (such as COOH and OH) [18,19]. The covalent bands can be used as the electron transfer channels between metalloporphyrins and photocatalysts and can further give rise to better selectivity and/or efficiency in catalytic processes [20–23]. Indeed, due to its two-dimensional flexible structure, g-C_3N_4 may be easily modified with organic small molecules as a promising photocatalyst [24–33]. Accordingly, on the basis of the latent characteristics of metalloporphyrins, it can be anticipated that the combination between g-C_3N_4 and metalloporphyrins could be supported to provide a synergistic effect of enhancing the photocatalytic activity with considerable visible light utilization efficiency.

In this work, tetra(4-carboxyphenyl)porphyrin (TCPP), FeTCPP, and CNNS were successfully prepared firstly. Different mass contents of FeTCPP were introduced on the surface of g-C_3N_4 nanosheets, forming FeTCPP@CNNS photocatalysts by π–π stacking interactions and hydrogen bonding. Illustrated in Figure 1, the photocatalysts were fabricated by integrating FeTCPP with g-C_3N_4 sheets via a mechanical mix method. The FeTCPP acts as the light-harvesting part, and CNNS as the catalytic center, which can accelerate the separation rate of the photogenerated electron and hole carriers. Under visible light irradiation, the sensitized photocatalysts 3% FeTCPP@CNNS shows a high photocatalytic activity for 4-NP degradation due to the efficient transfer to CNNS of the photogenerated electrons of the excited FeTCPP. On the basis of the results of the active radical identification experiments, the possible photocatalytic mechanism for the TCPP/CNNS composites was also elucidated. This work shows that CNNS sensitized by FeTCPP could enhance the photocatalytic degradation of 4-NP for more efficiently utilizing solar radiation.

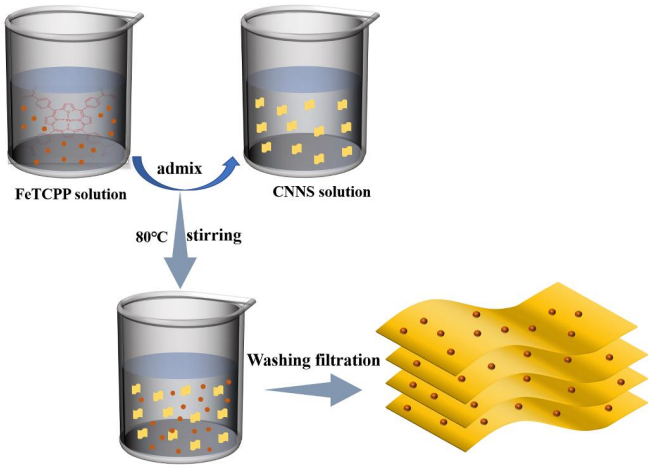

Figure 1. Schematic illustration of preparation process for FeTCPP@CNNS.

2. Results and Discussion

Figure 2a displays the X-ray diffraction pattern of the prepared materials. It can be found from Figure 2a that the bulk g-C_3N_4 presents peaks at 12.8° and 27.7°, corresponding to the (100) crystal plane and (002) crystal plane of g-C_3N_4, respectively. The peak at 12.7° is weak, which reflects the regular arrangement of triazine rings in g-C_3N_4, and the peak strength is strong at 27.5°, which reflects the typical graphite interlayer stacking structure [34,35]. Compared with bulk g-C_3N_4, the peak (002) of CNNS became wider and slightly more weakened, indicating that the crystallinity of CNNS was not as good as bulk g-C_3N_4. Meanwhile, the peak (100) of CNNS almost disappeared, indicating that the nanosheet was successfully exfoliated [8]. FeTCPP has a very wide diffraction peak at approximately 21.4°, indicating that TCPP has an amorphous structure [16]. Figure 2b shows the X-ray diffraction of FeTCPP@CNNS materials and CNNS. It can be found that when CNNS is sensitized by a small amount of FeTCPP, the peak (002) generated by interlamellar deposition of graphite is slightly larger than that of pure CNNS. It is caused by the interaction between CNNS and FeTCPP through the triazine unit of porphyrin [36]. No obvious characteristic peak of FeTCPP was observed in FeTCPP@CNNS composites, on the one hand, because of the low content of FeTCPP in the composites, and on the other hand, because of the weak peak width of the diffraction characteristics of FeTCPP [37]. By further comparison, it can be observed that the XRD spectra of composites are very similar to those of the CNNS monomer, which also indicates that the addition of FeTCPP will not damage the crystal structure of CNNS [38].

Figure 2c,d show FTIR spectra of TCPP, FeTCPP, CNNS, and FeTCPP@CNNS. FTIR spectra of TCPP and FeTCPP are reflected in Figure 2c, where the characteristic peak at 963 cm^{-1} represents the N-H telescopic vibration pattern on the pyrrole ring of TCPP [39]. This feature peak disappears in the FTIR spectrogram of FeTCPP. In addition, a new characteristic peak at 1001 cm^{-1} can be observed in the FTIR spectrum of FeTCPP, which indicates that after the metal ions enter the porphyrin ring, the deformation vibration of the ring is enhanced. In addition, the telescopic vibration characteristic peak of Fe-N is generated, which demonstrates that the porphyrin ligand with the metal ion can form the complex [38]. For FeTCPP materials, the characteristic peaks at 1276, 1405, and 1604 cm^{-1} belong to the -OH tensile vibration in -COOH, the C-N in-plane vibration of pyrrole. The tensile vibration of C-C at 1710 cm^{-1} indicates the telescopic vibration absorption of the -COOH and -NH_2 functional groups in their molecular structures [39,40]. In Figure 2d, for pure CNNS, the spike absorption peak at 809 cm^{-1} is attributed to the typical vibration pattern of the graphite phase carbon nitride triazine ring, and the presence of four more obvious characteristic absorption peaks in the range of 1700−1200 cm^{-1} is due to the telescopic vibration of the surface C-N heterocyclic ring [41,42]. In the FTIR spectra of the FeTCPP@CNNS, it can be observed that the characteristic peaks are almost consistent with those of pure CNNS, which demonstrate that the structure of CNNS has not changed during mechanical stirring. The -NH_2 deformation vibration band at 1573 cm^{-1} in the CNNS monomer disappeared in the FeTCPP@CNNS composite because of the covalent formation of -N-O by the COOH of porphyrin and NH_2 of g-C_3N_4 [39]. The characteristic tensile bands of amide groups formed between metalloporphyrin and g-C_3N_4 at 1640 and 1260 cm^{-1} were not clearly observed, possibly because that the peaks were too small and similar to the peaks of pure CNNS. The results confirm that the hybrid effect between FeTCPP and CNNS molecules may come mainly from non-covalent interactions [14].

The UV-visible diffuse reflection spectra of CNNS, FeTCPP, and FeTCPP@CNNS composites are exhibited in Figure 3a; it can be seen that pure CNNS has an absorption edge at 450 nm, and the DRS spectra of FeTCPP@CNNS composites also exhibit the absorption characteristic peaks of CNNS. As illustrated in the DRS spectrum of FeTCPP, there is an absorption peak at 403 nm, related to the Soret band (B band) of the porphyrin compound, and absorption peaks at 520 nm, 578 nm, and 693 nm, corresponding to the Q band of the porphyrin compound [43,44]. With the increasing content of FeTCPP, the absorption characteristic peak of the FeTCPP@CNNS composites is slightly enhanced. As shown in

Figure 3a, there is a slight redshift phenomenon indicating that there was a π-π interaction between CNNS and FeTCPP [38] and further illustrating the successful formation of FeTCPP@CNNS composites. Figure 3b shows the band gap according to the Kubelka Munk transform [45]: $(\alpha hv)^2 = A(hv - Eg)$. The corresponding band gap of CNNS and FeTCPP are, respectively, calculated to be approximately 2.74 eV and 2.01 eV. The band gap of 3% FeTCPP@CNNS composite material is the smallest one at approximately 2.36 eV, illustrating that the 3% FeTCPP@CNNS composite can mostly improve the utilization rate of visible light.

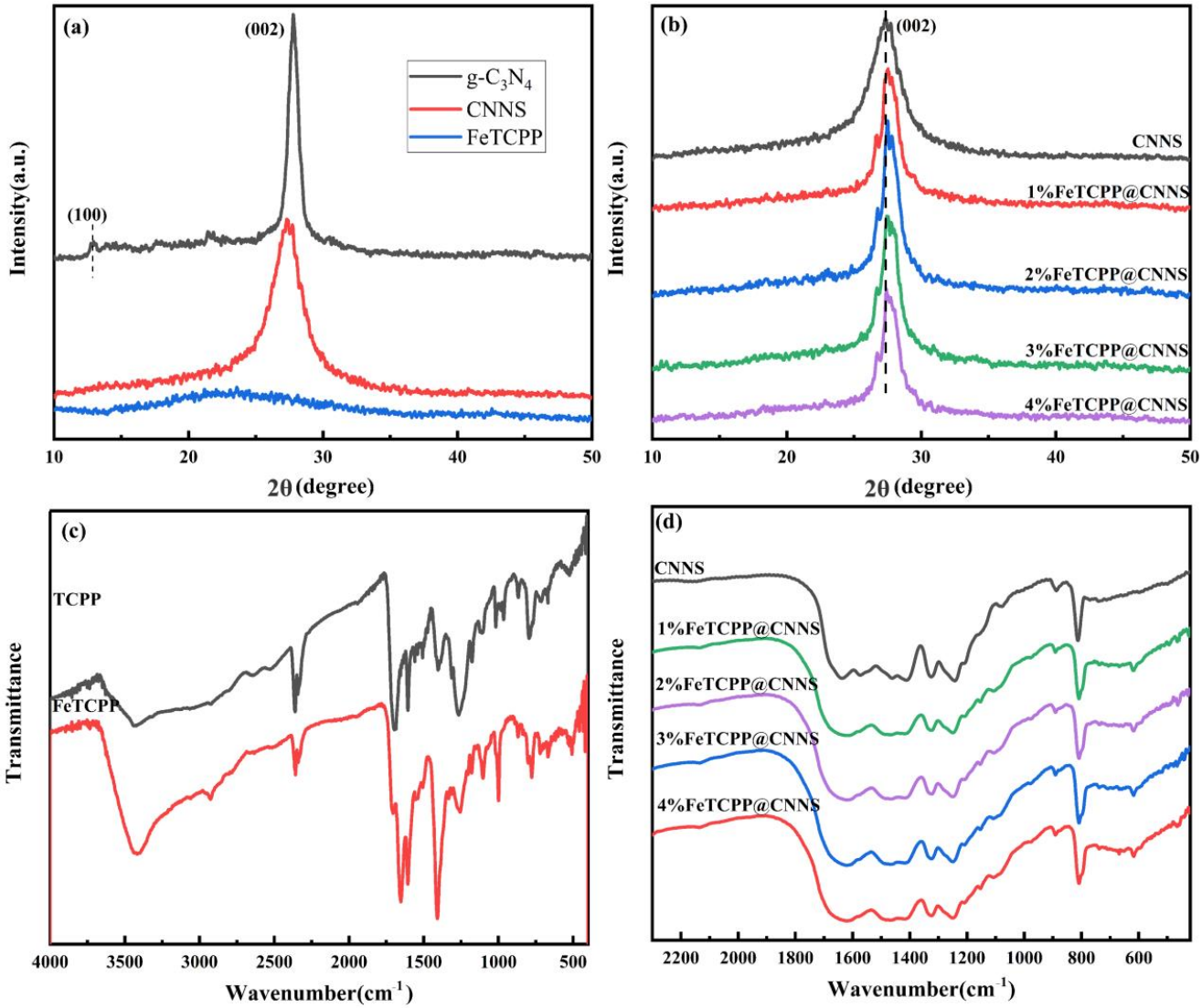

Figure 2. XRD spectra of (**a**) g-C_3N_4, CNNS, and FeTCPP and (**b**) FeTCPP@CNNS composites; FTIR spectra of (**c**) TCPP and FeTCPP and (**d**) CNNS and FeTCPP@CNNS composites.

The typical SEM images and EDS patterns of as-prepared samples are shown in Figure 4. In Figure 4a, it can be seen that the FeTCPP presents an irregular small particle shape. Figure 4b,c are SEM images of CNNS and 3% FeTCPP@CNNS. The CNNS sample presents a thin sheet-shaped morphology with a wrinkle, facilitating the transport of electrons. With only a small amount of FeTCPP introduced, as shown in Figure 4c, the stacked lamellar structure is displayed. FeTCPP is deposited on the surface of CNNS. In Figure 4d, the C:N atomic ratio is approximately 1:1, higher than that of g-C_3N_4 (3:4), which indicates that FeTCPP has been successfully loaded onto CNNS [16]. The elemental mapping of the 3% FeTCPP@CNNS composite shown in Figure 4e–h reveals a uniform

distribution of C, N, O, and Fe elements in the 3% FeTCPP@CNNS framework, highlighting the C, N, O, and Fe co-doped nature of the 3% FeTCPP@CNNS composite.

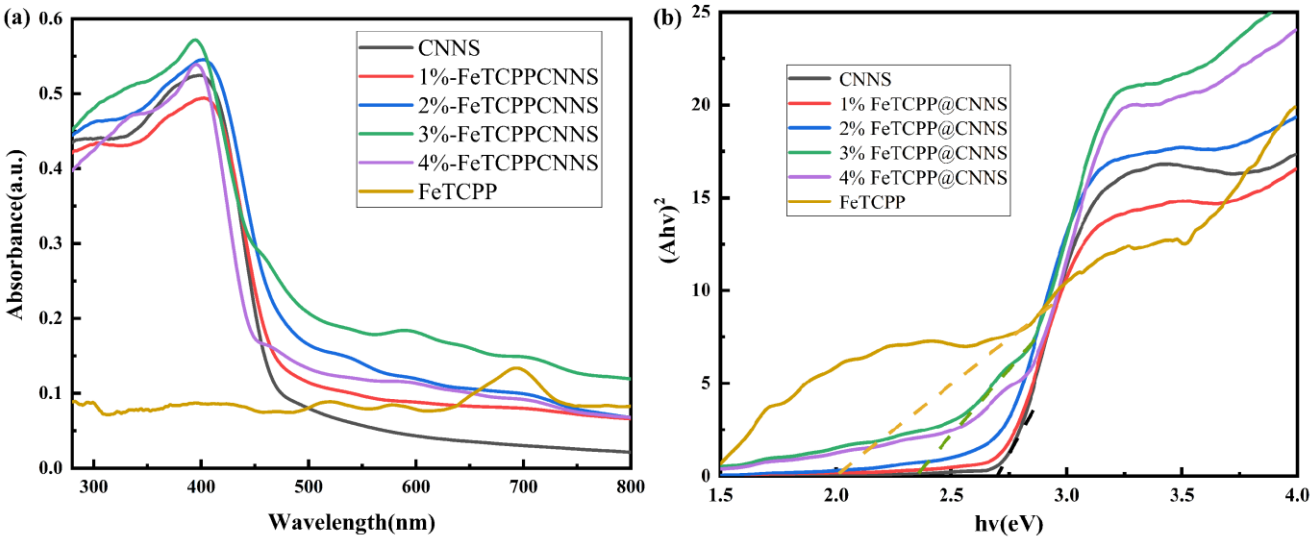

Figure 3. (**a**) UV-vis diffuse reflection spectra and (**b**) the band gap determined from Kubelka Munk transformation of CNNS, FeTCPP, and FeTCPP@CNNS composites.

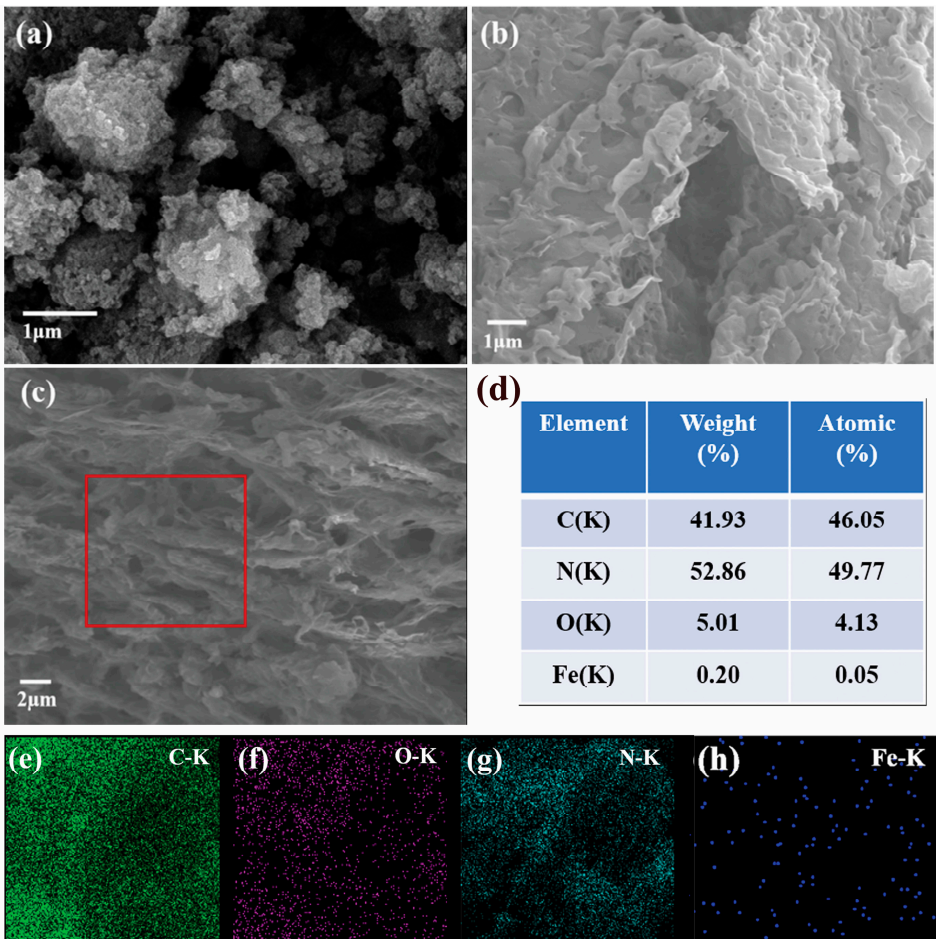

Element	Weight (%)	Atomic (%)
C(K)	41.93	46.05
N(K)	52.86	49.77
O(K)	5.01	4.13
Fe(K)	0.20	0.05

Figure 4. SEM images of (**a**) FeTCPP, (**b**) CNNS, and (**c**) 3% FeTCPP@CNNS; (**d**) EDS at 3% FeTCPP@CNNS (red area in figure (**c**)); (**e**–**h**) The corresponding EDS elemental mapping of C, O, N, and Fe elements in 3% FeTCPP@CNNS composites.

In order to further investigate the chemical composition and surface element valence states of FeTCPP@CNNS composite, X-ray photoelectron spectroscopy (XPS) analysis of 3% FeTCPP@CNNS composite is carried out. For comparison, the composition of CNNS and FeTCPP are also determined by XPS measurement. As shown in Figure 5a, C, N, and O signals are detected in the CNNS sample, while C, N, O, and Fe signals are detected in the FeTCPP sample. In the 3% FeTCPP@CNNS composite, the corresponding C, N, O, and Fe signals are found. The results show that the FeTCPP sample is successfully introduced in the composite material. Figure 5b–e show the spectra of C 1s, N 1s, O 1s, and Fe 2p, respectively. Figure 5b shows the C 1s spectra of CNNS and 3% FeTCPP@CNNS. There are two primary peaks at 284.6 eV and 288.2 eV, corresponding to the C-C bond of graphite and the Sp^2 hybrid carbon in the N=C-N aromatic ring [46,47]. Figure 5c shows the N 1s spectra of CNNS and 3% FeTCPP@CNNS materials. In the N 1s spectrum of CNNS, the peaks at 398.2 eV, 399.3 eV, and 401 eV correspond to C-N=C bond, (N-(C)3) bond, and secondary amino (C-N-H) bond, respectively [48,49]. The three peaks can also be observed in 3% FeTCPP@CNNS; however, the peak of C-N=C bond shifted to higher binding energy by 0.6 eV, and the peak of CN-H shifted to lower binding energy by 0.4 eV, which should be caused by the formation of type-II heterojunction photocatalyst [50] FeTCPP@CNNS. The O 1s spectra are shown in Figure 5d. The peak at 531.9 eV can be attributed to the -OH group, which means that only -OH forms on the surface due to the combustion of g-C_3N_4 in air [16,41]. The Fe 2p spectra of FeTCPP materials are shown in Figure 5e. The two peaks at 710.7 and 724.1 eV correspond to Fe 2p1/2 of Fe 2p3/2 and Fe^{3+} at octahedral positions, respectively [51–53]. However, no obvious Fe 2p peak was detected in 3% FeTCPP@CNNS, which may be because the low content of Fe doped in the composite and wrapped in porphyrin molecules.

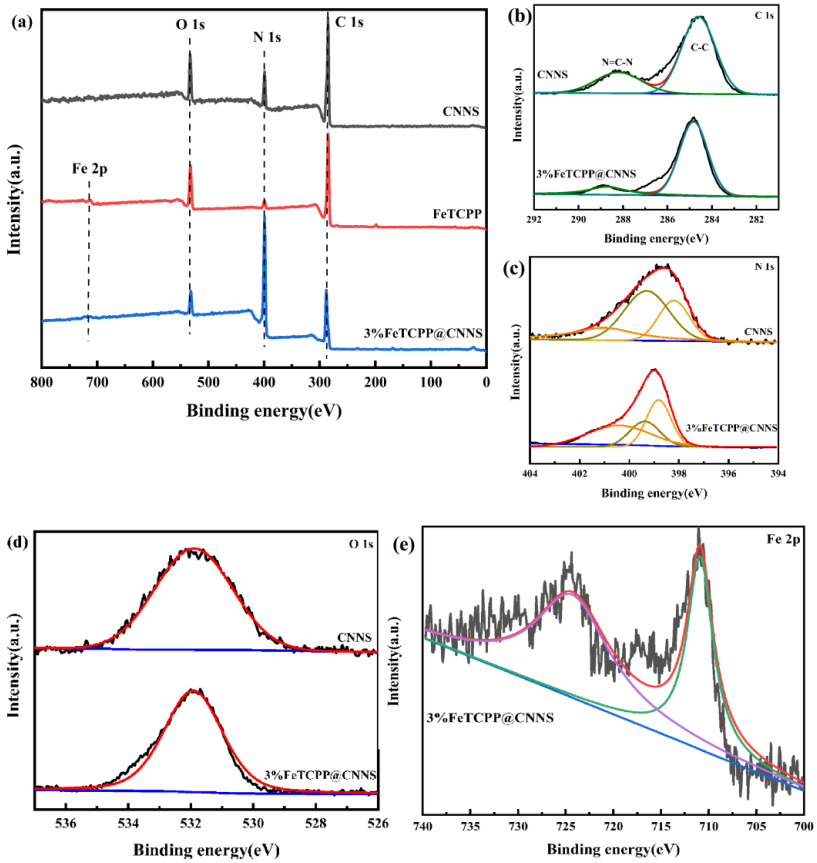

Figure 5. (**a**) XPS survey of CNNS, FeTCPP, and 3% FeTCPP@CNNS, (**b**) C 1s spectra, (**c**) N 1s spectra, (**d**) O 1s spectra of CNNS and 3% FeTCPP@CNNS, and (**e**) Fe 2p spectra of 3% FeTCPP@CNNS.

Figure 6 shows that the N_2 adsorption–desorption isotherms of CNNS and 3% FeTCPP@CNNS composite materials are similar and belong to the type IV isotherm, which manifests that both materials display mesoporous structures [54]. Additionally, the specific surface area (S_{BET}), average pore size, and pore volume of all samples are presented in Table 1. The BET surface area of CNNS and 3% FeTCPP@CNNS composite are approximately 11.8 and 24.9 m^2 g^{-1}, respectively. Compared with CNNS, the 3% FeTCPP@CNNS composite has a larger specific surface area, indicating that it can provide more active sites and promote the transport and separation efficiency of photogenerated carriers [55], thus further improving the utilization of light.

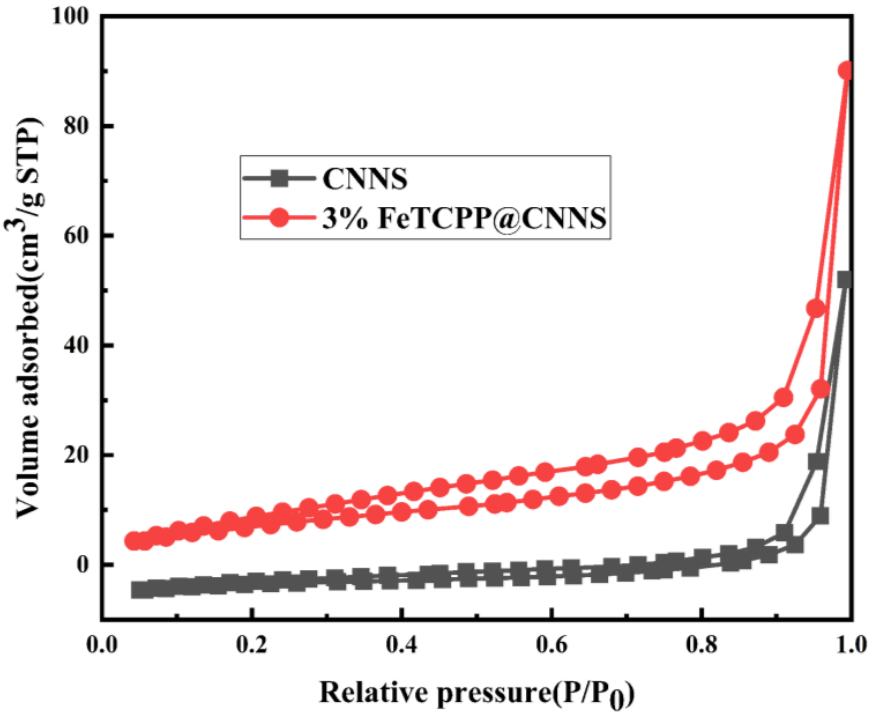

Figure 6. N_2 adsorption–desorption isotherms curves of CNNS and 3% FeTCPP@CNNS.

Table 1. Specific surface, pore characteristics, and crystallite sizes of the as-prepared samples.

Samples	SBET (m^2g^{-1})	Pore Volume (cm^3g^{-1})	Pore Size (nm)
CNNS	11.8	0.064	21.8
3% FeTCPP@CNNS	24.9	0.100	16.1

The photoluminescence spectra of CNNS, FeTCPP, and FeTCPP@CNNS composites are depicted in Figure 7a at an excitation wavelength of 320 nm. As reported [56], the weak PL emission peak indicates that the separation efficiency of the photoexcitation electron-hole pair is higher, resulting in higher photocatalytic performance. It can be found that CNNS and FeTCPP@CNNS composites show emission peaks in the region from 420 nm to 440 nm, while pure FeTCPP has no obvious emission peaks [36]. CNNS shows the strongest emission peak in the region from 440 nm to 550 nm, demonstrating the highest recombination rate of photogenerated photoelectrons and holes on the materials' surface. With a certain content of FeTCPP, it can inhibit the recombination of photogenerated carries in CNNS. With the increasing content of FeTCPP, the PL intensity of FeTCPP@CNNS composites decreases gradually. The 3% FeTCPP@CNNS exhibits the weakest PL intensity. However, when the content of FeTCPP is further increased, the PL intensity becomes slightly stronger, indicating that the appropriate content of FeTCPP can enhance the charge transfer efficiency.

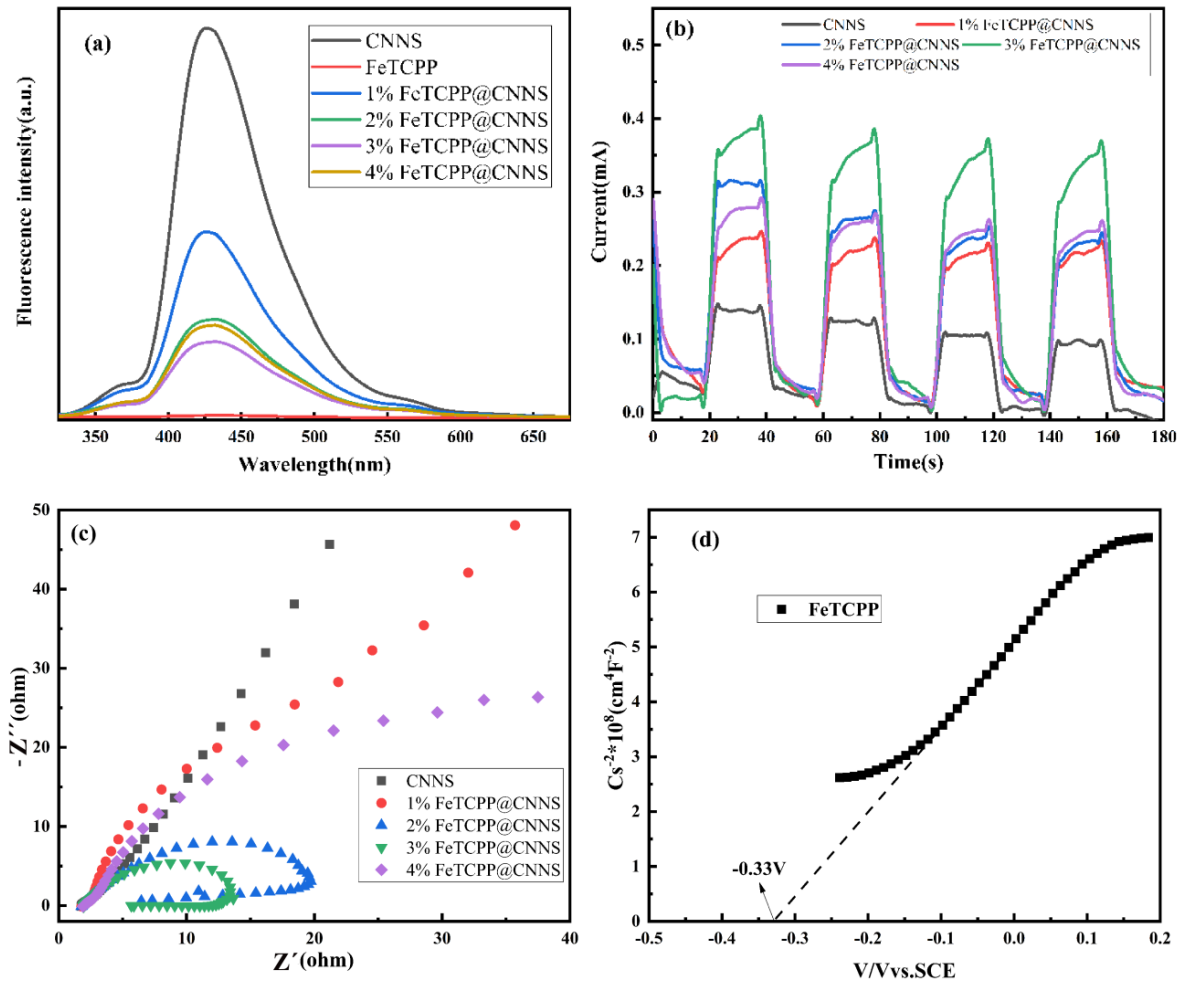

Figure 7. (**a**) PL spectra of CNNS, FeTCPP, and FeTCPP@CNNS composites, (**b**) photocurrent response diagram, (**c**) EIS spectra of CNNS and FeTCPP@CNNS composites, and (**d**) Mott-Schottky plot of FeTCPP.

To further study the electron transfer process, the photocurrent response of CNNS and FeTCPP@CNNS composites are measured, as shown in Figure 7b. Obviously, the photocurrent intensity of all samples increases sharply after the light irradiation is turned on, and when the irradiation is interrupted, it drops sharply to zero. The results indicate that they all have photocatalytic capability. The higher photocurrent intensity indicates more efficient separation of photogenerated carries. Among them, the photocurrent intensity of 3% FeTCPP@CNNS composite is the highest. In addition, the photocurrent intensity of 3% FeTCPP@CNNS composite exhibits approximately 0.4 μA under simulated sunlight, which is twice more than that of the pure CNNS photocatalyst. It indicates that the 3% FeTCPP@CNNS composite could effectively improve the separation and transfer of photogenerated carries under visible light. The stability of the photocurrent response of all the prepared samples is determined by intermittent illumination for 20 s multiple cycles. It shows that there is only a slight reduction in the photocurrent intensity after four cycle operations, resulting in prepared samples that have good stability. Figure 7c presents electrochemical impedance spectroscopy. The minimum arc radius of the 3% FeTCPP@CNNS composite indicates the lowest interfacial resistance. Meanwhile, spectral line of CNNS has the largest slope in the low frequency region, indicating the largest diffusion resistance of CNNS [9,57]. The 3% FeTCPP@CNNS composite exhibits excellent charge separation, which is consistent with the above photocurrent results. In Figure 7d, the Mott–Schottky (MS) plot of FeTCPP is recorded by an electrochemical analyzer. The

flat band potential (E_{fb}) of FeTCPP is −0.39 eV (vs. SCE). The E_{CB} of FeTCPP is −0.35 eVB based on the formula [58]: $E_{CB(NHE,pH=7)} = E_{fb(SCE,pH=7)} + 0.24 - 0.2$.

In Figure 8a, the degradation of 4-NP was negligible without photocatalysts, showing that 4-NP has almost no degradation by only direct visible light irradiation. A 50 mg catalyst is added to the 4-NP solution (20 mg L^{-1}) in the dark for 30 min to achieve adsorption–desorption equilibrium. After 60 min of illumination, it can be observed that the corresponding photodegradation efficiency of CNNS, 1% FeTCPP@CNNS, 2% FeTCPP@CNNS, 3% FeTCPP@CNNS, and 4% FeTCPP@CNNS are 37.2%, 63.7%, 77.9%, 92.4%, and 76.3%, respectively, as shown in Figure 8c. Compared with other photocatalysts, this shows that when the content of FeTCPP reaches 3%, the photodegradation efficiency reaches a maximum of 92.4% in 60 min. After the first-order kinetic equation fitting, it shows that the largest constant value of 3% FeTCPP@CNNS (k) is 0.037 min^{-1}, which is approximately 5 times that of CNNS. The results show that after being sensitized by FeTCPP, the FeTCPP@CNNS can quickly capture the visible light source and more easily produce photogenerated electrons under the illumination by visible light. Moreover, the separation rate of photogenerated electrons and holes is improved, resulting in effectively improved photocatalytic efficiency. As shown in Figure 8d, the absorbance of 4-NP significantly decreased with the increased illumination time. For comparison, recent photocatalysis performances of g-C_3N_4-based and TCPP-based materials under visible light irradiation are shown in Table 2. This information reveals that the 3% FeTCPP@CNNS exhibits higher photodegradation efficiency and higher degradation rate constants.

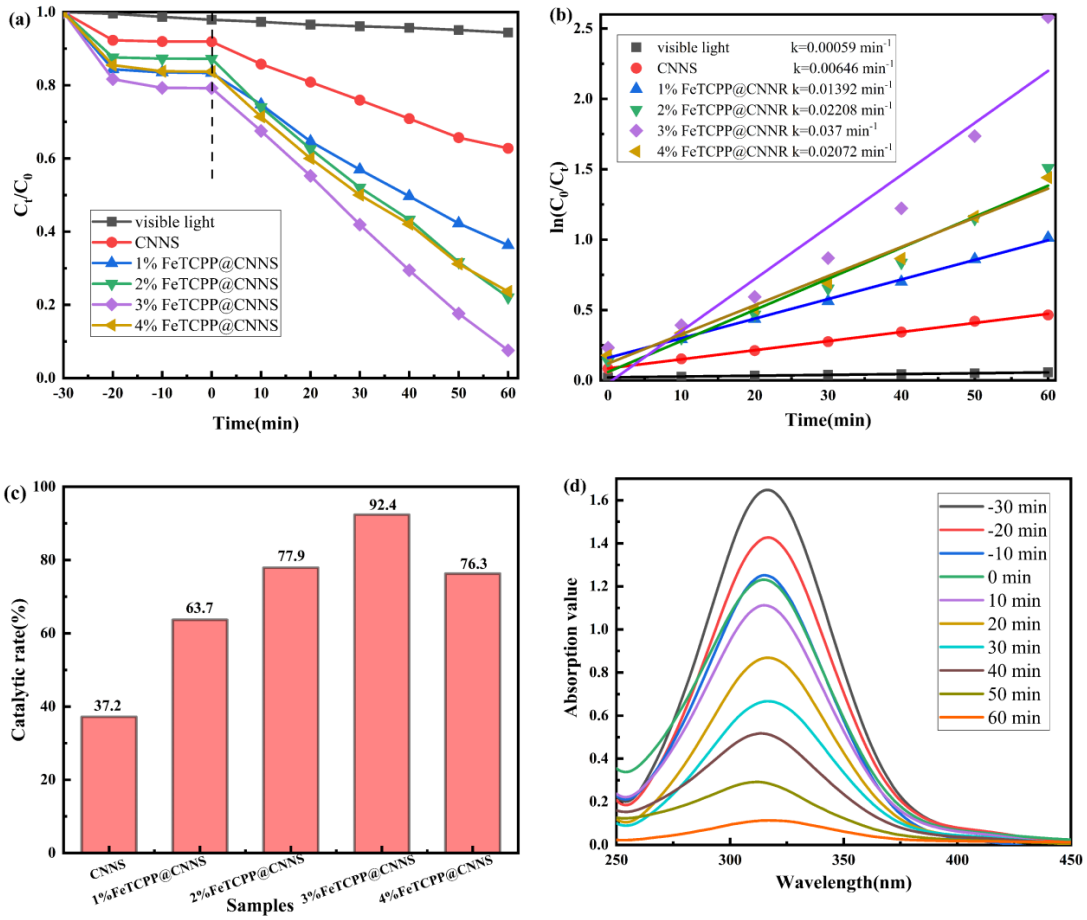

Figure 8. (**a**) Photocatalytic degradation for 4-NP aqueous solution over different photocatalysts under simulated solar light irradiation, (**b**) kinetics curves, (**c**) photodegradation efficiency of the as-prepared samples, and (**d**) temporal UV-vis absorption spectral changes of 4-NP in aqueous solution with presence of 3% FeTCPP@CNNS composite during the photocatalytic degradation.

Table 2. Some reported materials based on g-C_3N_4 or TCPP studied for photocatalysis under visible light irradiation in recent years.

Composite	Catalyst Dose	Concentration	Light Source	Degradation and Time (%)	Degradation Rate Constant (k)
TCPP/$ZnFeO_4$@ZnO [59]	50 mg	10 mg/L, 50 mL (4-NP)	5 W LED lamp	67% in 3 h	–
g-C_3N_4@MoS_2/TiO_2(CMT10) [60]	50 mg	1×10^{-5} mol/L (4-NP)	500 W tungsten halogen lamp	78% in 1 h	–
g-C_3N_4/$CoFe_2O_4$ [61]	25 mg	20 mg/L (4-NP)	Visible-light	–	0.0156 min^{-1}
g-C_3N_4-30%@Ti-MIL125 [62]	–	–	Visible-light	75% in 4 h	–
1 $ZnFe_2O_4$/g-C_3N_4 [63]	50 mg	20 mg/L, 100 mL (4-NP)	Sunlight	–	0.02876 min^{-1}
0.4 S/Cl-g-C_3N_4 [64]	50 mg	5 mg/L, 100 mL (4-NP)	Xenon lamp	–	0.0095 min^{-1}
30% ZrO_2/g-C_3N_4 [65]	360 mg	30 mg/L, 100 mL (4-NP)	300 W Xe	–	0.0167 min^{-1}
0.75% CuTCPP/g-C_3N_4 [14]	25 mg	5 ppm, 50 mL (phenol)	500 W Xe	–	0.024 h^{-1}
3% FeTCPP@CNNS in this work	20 mg	20 mg/L, 100 mL (4-NP)	150 W Xe	94.2% in 1 h	0.037 min^{-1}

In order to evaluate the photocatalytic stability of the 3% FeTCPP@CNNS composite, the cycle test of it is performed five times, as shown in Figure 9a. After five cycling experiments, the photocatalytic activity remains the same. In addition, there is no obvious difference in XRD patterns of the prepared 3% FeTCPP@CNNS and the used one after five cycles. Therefore, the 3% FeTCPP@CNNS sample exhibits excellent degradation performance and possesses high stability under visible light.

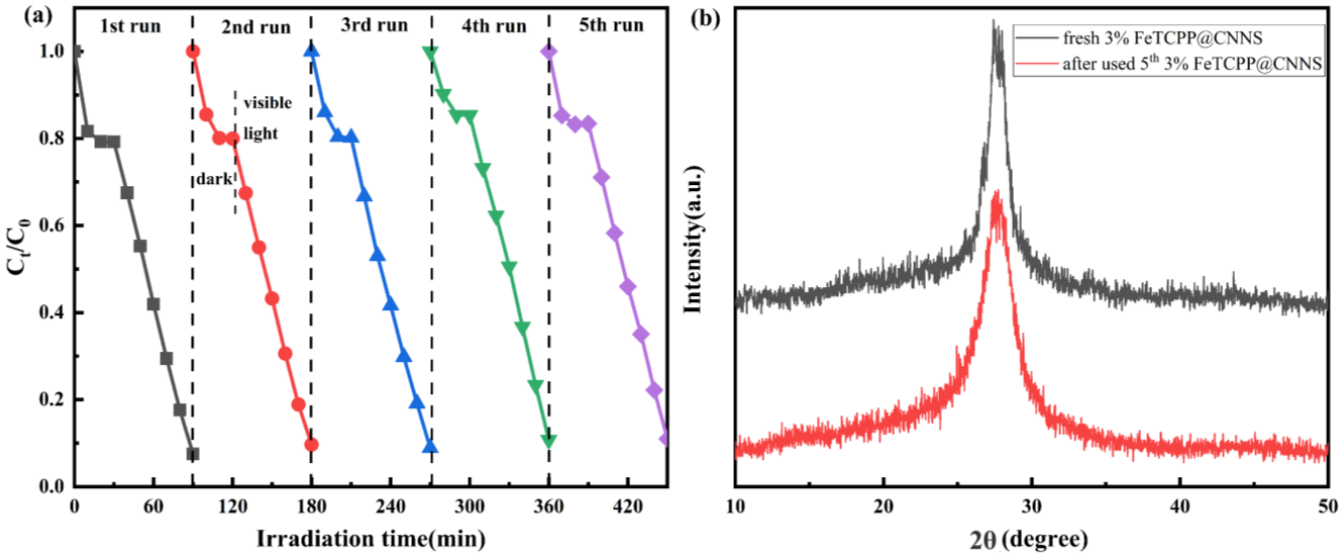

Figure 9. The 3% FeTCPP@CNNS photocatalytic degradation of 4-NP (**a**) cycle test curve and (**b**) XRD contrast after 5 cycles.

To further explore the reaction mechanism of the 3% FeTCPP@CNNS composite, the reactive species are determined in 1 mmol p-benzoquinone (BQ), isopropanol (IPA), and disodium edetate (EDTA-2Na), which were treated as superoxide radicals ($\cdot O^{2-}$), hydroxyl radicals ($\cdot OH$), and an inhibitor of the photo-excited hole (h^+), respectively [66]. From Figure 10a, the addition of IPA and EDTA-2Na inhibitors had little effect on the photocatalytic activity of the 3% FeTCPP@CNNS photocatalyst, and the addition of BQ significantly inhibited its photocatalytic activity. These results mean that $\cdot O^{2-}$ is the main substance for photocatalytic degradation of 4-NP.

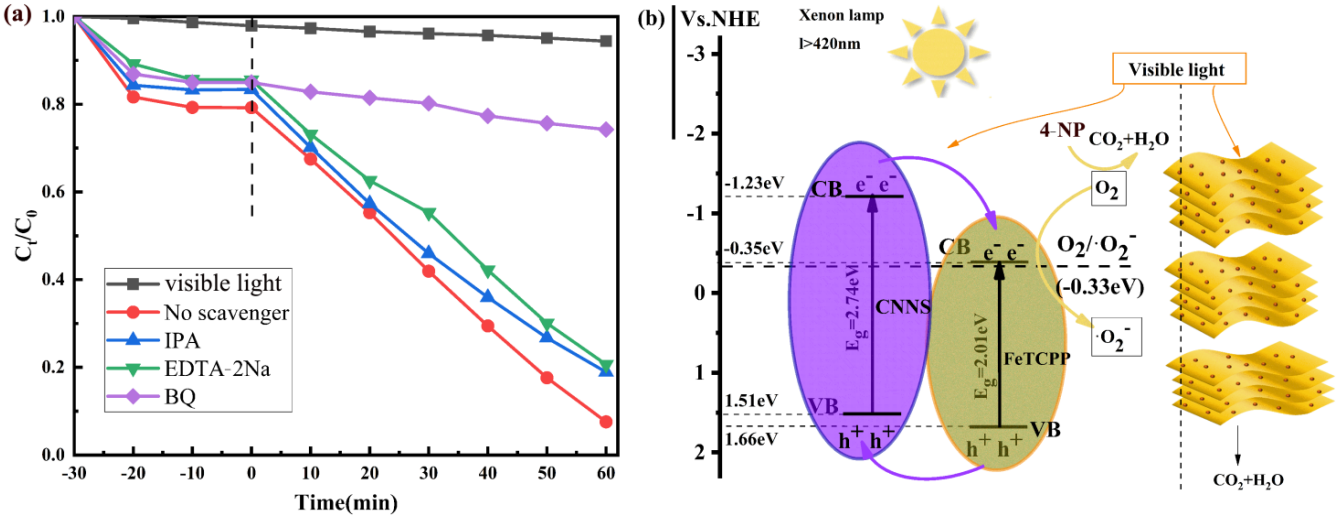

Figure 10. (**a**) Active substance capture experiment of 3% FeTCPP@CNNS photocatalyst under visible light irradiation and (**b**) photocatalytic mechanism of FeTCPP@CNNS photocatalyst under visible light irradiation.

The photocatalytic degradation capacity of pure CNNS and FeTCPP@CNNS composites are evaluated by using 4-NP as a contaminant according to the formula:

$$\eta = (1 - C_t/C_0) \times 100\%$$

The photodegradation rate (η) is known. At the same time, the adsorption experimental data conform to the pseudo-first-order model:

$$\ln(C_t/C_0) = kt$$

where C_0 and C_t signify initial concentration and instantaneous concentration within the reaction time t, respectively. k is the first-order reaction rate constants [67].

To further account for the photocatalytic mechanism, the band gap potential of the sample needs to be tested, and the conduction band (*CB*), the valence band (*VB*) position of CNNS, and the valence band (*VB*) position of FeTCPP are estimated using the following formulas [68]:

$$E_{VB} = \chi - E^e + 1/2E_g$$

$$E_{CB} = E_{VB} - E_g$$

where χ is electronegativity, E_{VB} and E_{CB} denote *VB* and *CB* marginal potentials, respectively, E_g denotes the energy band gap, E_e represents the energy of free electrons at the hydrogen scale (approximately 4.5 eV vs. NHE) [69], χ is the geometric mean of the constituent atoms, and g-C_3N_4 is 4.64 eV [70]. According to the above analysis, the E_{VB} and E_{CB} of CNNS are calculated, respectively, to be 1.51 eV and −1.23 eV. Through DRS and MS tests, the FeTCPP E_g is 2.01 eV and the E_{CB} is −0.35 eV, so that the E_{VB} of FeTCPP is 1.66 eV. Relying on the above experimental results, a possible photocatalytic mechanism is proposed and demonstrated in Figure 10b. Under visible light illumination, CNNS can form a photogenerated electron–hole pair under the excitation of visible light. Because the E_{CB} edge and E_{VB} edge charges of FeTCPP are smaller than those of CNNS, parts of the photosensitive electrons (e^-) at the *CB* position of CNNS can migrate to the *CB* of FeTCPP, and parts of the photosensitive electrons (e^-) at the *CB* position of CNNS can also be captured and generated by nearby O_2. At the same time, $\cdot O^{2-}$ reacts with 4-NP to decompose into CO_2 and H_2O [36], and photogenerated h^+ can be transferred from the *VB* of FeTCPP to the *VB* of CNNS, reducing the chance of recombination of photogenerated e^--h^+ pairs,

which can effectively improve photocatalytic activity. Furthermore, the improvement on the photocatalytic performance is also related to the photo-Fenton effect, as reported in previous reports [71,72].

3. Experimental Section

3.1. Materials

Melamine ($C_3H_6N_6$), ethanol (C_2H_6O), ethylene glycol ($C_2H_6O_2$), barium sulfate ($BaSO_4$), anhydrous sodium sulfate (Na_2SO_4), Carboxy benzaldehyde ($C_8H_6O_3$), propionic acid (CH_3CH_2COOH), pyrrole (Py), methanol (CH_3OH), N-N dimethylformamide (DMF)), ferric chloride hexahydrate ($FeCl_3 \cdot 6H_2O$), isopropyl alcohol (IPA), and EDTA-2NA were purchased from China, Shanghai Sinopharm Chemical Reagents Co., Ltd.; Nitric acid (HNO_3) was ordered from China, Shanghai Suyi Chemical Reagent Co., Ltd.; and Para-benzoquinone ($C_6H_4O_2$) was ordered from China, Shanghai Maclin Biochemical Technology Co., Ltd. All chemicals used in this experiment are reagent grade and were used as received.

3.2. Synthesis of FeTCPP

Tetracarboxylic phenyl porphyrin was synthesized by the Adler method [73]. Firstly, Carboxy benzaldehyde (2 g) and propionic acid (150 mL) were mixed, being stirred in a three-neck flask equipped with reflux condenser at 135 °C. Pyrrole (1 mL) was dissolved in 20 mL propionic acid, which was added drop by drop into the upper reaction solution over 1 h. The reaction solution was refluxed for 2 h. The propionic acid was removed under vacuum and then the residue was dispersed in $CHCl_3$, filtered, and washed. The remaining solid powder was dissolved in the mixture solvent (propionic acid/$CHCl_3$ with 3:2 volume), and the insoluble portion was removed by filtration. Using propionic acid/$CHCl_3$ (3:2, v/v) as eluent, the mixture was separated by chromatography on silica gel column. The first colored band was collected concentrated and dried. The resulting product was tetracarboxylic phenyl porphyrin, labelled as TCPP.

TCPP (0.5 g) and $FeCl_3 \cdot 6H_2O$ (1 g) in 100 mL DMF were dissolved in DMF, and then heated to 150 °C for 3 h with stirring. DMF was removed under vacuum after cooling to room temperature. The remaining solid was dissolved in ethanol, and insoluble impurities were removed via filtration. By rotary evaporation, the residue was dried. The obtained composites were labelled as FeTCPP.

3.3. Synthesis of CNNS

Bulk g-C_3N_4 was prepared first. Then, 5 g melamine powder was mixed with ethylene glycol (120 mL) by ultrasonication for 2 h, and then dilute nitric acid (120 mL, 0.36 mol L^{-1}) was added to the above mixture solution under stirring. The sediment was washed and dried after stirring for 12 h. The obtained powder was heated to 550 °C for 4 h at a heating rate of 5 °C/min in a muffle furnace. Then, the bulk g-C_3N_4 was obtained. As previously reported, the g-C_3N_4 nanosheets were produced by thermal oxidation etching of bulk g-C_3N_4 directly at 550 °C for 2 h [36]. The obtained light yellow powder was dried at 60 °C for 12 h in a vacuum oven and was named CNNS.

3.4. Preparation of FeTCPP@CNNS

Typically, CNNS powder (1 g) was dispersed in 50 mL ethanol by ultrasonication. Then, a certain amount of FeTCPP was added to ethanol (10 mL), and the mixture was mixed into the above solution with magnetic stirring at 80 °C. Then, FeTCPP@CNNS composite material was obtained. The preparation process of FeTCPP@CNNS materials are shown in Figure 1. By this method, FeTCPP@CNNS composites with different FeTCPP contents (10 mg, 20 mg, 30 mg, and 40 mg) were prepared, which were denoted as X% FeTCPP@CNNS (X% = 1%, 2%, 3%, and 4%).

3.5. Photocatalytic Assessment

The photocatalytic degradation of 4-NP was studied using xenon lamp (150 W) with filter as visible light source. Here, 50 mg photocatalyst was dispersed by magnetic stirring into 100 mL 4-NP aqueous solution (20 mg L^{-1}). Firstly, the adsorption–desorption equilibrium was obtained by ultrasound for 0.5 h in the dark, then under visible light, and the reaction mixture was irradiated for 1 h. Then, 5 mL of the mixture was removed from the reactor, and at the same time interval, the concentration of 4-NP was determined by UV-Vis spectrophotometer.

During the photocatalytic degradation of 4-NP, the effect of reactive oxygen species on the best-performing photocatalyst was tested for a scavengers, namely P-benzoquinone (BQ), isopropanol (IPA), and ethylenediamine tetraacetic acid disodium salt (EDTA-2Na). For this test, 1 mM scavenger was, respectively, added into 100 mL 4-NP solution (20 mg L^{-1}), then was added 20 mg of catalyst. An additional procedure was carried out, which was the same as the process but without scavengers. Thus, all experiments were conducted under the identical conditions.

3.6. Description of the Characteristics

XRD-600 (Rigaku, Japan) was used to determine the crystal phase of X-ray samples. FTS2000 (Thermos, Waltham, MA, USA) Fourier infrared spectrometer was used for qualitative analysis of the chain structure of the samples. Using barium sulfate as blank samples, the samples were detected by diffuse reflectivity spectroscopy (DRS) spectrophotometer on UV-2550 (Shimadzu, Tokyo, Japan). Merlin Compact (Merlin, Forchtenberg, Germany) was used for obtaining the field emission scanning electron microscope (FESEM) images. The surface chemical composition of the samples was analyzed by X-ray photoelectron spectroscopy (XPS, Thermos Fish Scientific, USA). Nitrogen adsorption and desorption tests (BET) were measured at 77 k using the TA Instruments SDT Q600 analyzer (Quadrasorb, WI, USA). Quantachrome Instrument nitrogen adsorption device was used to record the adsorption and desorption isotherms. The photoluminescence spectrum was performed via Spectro fluorometer FS5 (Picoquant, Berlin, Germany) with a slit of 10 nm and an excitation wavelength of 320 nm. The prepared sample was considered to be the working electrode, a platinum wire to be a counter electrode, and a saturated Ag/AgCl electrode to be a reference electrode. Additionally, 0.5 mol L^{-1} aqueous solution of Na_2SO_4 was the electrolyte. Under the disturbance signal of 8 mV, electrochemical impedance spectroscopy (EIS) was measured in the frequency range of 1 MHz to 1000 MHz, and photocurrent test and electrochemical impedance–potential test were measured on the material. In addition, the MPC-3100 UV-NEAR infrared spectrophotometer (USA) was used for analyzing the degradation concentration of the sample.

4. Conclusions

In summary, the FeTCPP@CNNS photocatalysts with stacked lamellar structure have been successfully fabricated by an in situ hydrothermal self-assembly approach. The FeTCPP@CNNS composites exhibit higher photocatalytic efficiency and stability than CNNS by the photodegradation of 4-NP dyes. The photocatalytic degradation rate reached the maximum value of approximately 92.4% of 3% FeTCPP@CNNS.

The degradation rate constant of the 3% FeTCPP@CNNS photocatalyst is 0.037 min^{-1} (4-NP), which is 5 times that of CNNS, indicating that proper FeTCPP introduced into CNNS can effectively improve transformation of photoexcitation electrons and holes. In addition, the results of the active species trapping experiments for the photodegradation of 4-NP show that $\cdot O^{2-}$ plays a major role in photocatalytic reactions. A possible photocatalytic reaction mechanism of FeTCPP@CNNS composite for photocatalytic degradation of 4-NP has been proposed. This work enables the application of CNNS-based photocatalysis under sunlight irradiation in wastewater treatment.

Author Contributions: Conceptualization, J.L.; methodology, Y.G.; software, L.L.; investigation, M.A.; data curation, J.W.; writing—original draft preparation, L.Z.; writing—review and editing, S.L.; supervision, W.S.; funding acquisition, X.C. All authors have read and agreed to the published version of the manuscript.

Funding: This research was funded by Postgraduate Research and Practice Innovation Program of Jiangsu Province, China (SJCX21_1765 and SJCX22_1932); NCN, Poland (UMO-2020/39/B/ST8/02937); and NAWA, (2020 PPN/BEK/2020/1/00129/ZAS/00001). This research was also supported by the Open Research Fund of the State Key Laboratory of Polymer Physics and Chemistry, Changchun Institute of Applied Chemistry, Chinese Academy of Sciences (2022-06). We also appreciate the support of the funding project by National Natural Science Foundation of China: 22006057.

Data Availability Statement: All data generated or analyzed during this study are included in this published article.

Conflicts of Interest: The authors declare no conflict of interest.

References

1. Jin, X.; Zhou, X.; Sun, P.; Lin, S.; Cao, W.; Li, Z.; Liu, W. Photocatalytic degradation of norfloxacin using N-doped TiO_2: Optimization, mechanism, identification of intermediates and toxicity evaluation. *Chemosphere* **2019**, *237*, 124433. [CrossRef]
2. Wang, S.; Wang, F.; Su, Z.; Wang, X.; Han, Y.; Zhang, L.; Xiang, J.; Du, W.; Tang, N. Controllable Fabrication of Heterogeneous p-TiO_2 QDs@g-C_3N_4 p-n Junction for Efficient Photocatalysis. *Catalysts* **2019**, *9*, 439. [CrossRef]
3. Li, S.; Zhang, Q.; Liu, L.; Wang, J.; Zhang, L.; Shi, M.; Chen, X. Ultra-stable sandwich shaped flexible MXene/CNT@Ni films for high performance supercapacitor. *J. Alloys Compd.* **2023**, *941*, 168963. [CrossRef]
4. Li, S.; Zhang, L.; Zhang, L.; Guo, Y.; Chen, X.; Holze, R.; Tang, T. Preparation of Fe_3O_4@polypyrrole composite materials for asymmetric supercapacitor applications. *New J. Chem.* **2021**, *45*, 16011. [CrossRef]
5. Lu, S.; Weng, B.; Chen, A.; Li, X.; Huang, H.; Sun, X.; Feng, W.; Lei, Y.; Qian, Q.; Yang, M.Q. Facet Engineering of Pd Nanocrystals for Enhancing Photocatalytic Hydrogenation: Modulation of the Schottky Barrier Height and Enrichment of Surface Reactants. *ACS Appl. Mater. Interfaces* **2021**, *13*, 13044. [CrossRef] [PubMed]
6. Gao, M.; Zhou, W.-Y.; Mo, Y.-X.; Sheng, T.; Deng, Y.; Chen, L.; Wang, K.; Tan, Y.; Zhou, H. Outstanding long-cycling lithium−sulfur batteries by core-shell structure of S@Pt composite with ultrahigh sulfur content. *Adv. Powder Mater.* **2022**, *1*, 100006. [CrossRef]
7. Li, M.; Li, Z.; Wang, X.; Meng, J.; Liu, X.; Wu, B.; Han, C.; Mai, L. Comprehensive understanding of the roles of water molecules in aqueous Zn-ion batteries: From electrolytes to electrode materials. *Energy Environ. Sci.* **2021**, *14*, 3796. [CrossRef]
8. Asadzadeh-Khaneghah, S.; Habibi-Yangjeh, A.; Vadivel, S. Fabrication of novel g-C_3N_4 nanosheet/carbon dots/$Ag_6Si_2O_7$ nanocomposites with high stability and enhanced visible-light photocatalytic activity. *J. Taiwan Inst. Chem. Eng.* **2019**, *103*, 94. [CrossRef]
9. Gu, W.; Lu, F.; Wang, C.; Kuga, S.; Wu, L.; Huang, Y.; Wu, M. Face-to-Face Interfacial Assembly of Ultrathin g-C_3N_4 and Anatase TiO_2 Nanosheets for Enhanced Solar Photocatalytic Activity. *ACS Appl. Mater. Interfaces* **2017**, *9*, 28674. [CrossRef]
10. Pan, T.; Chen, D.; Xu, W.; Fang, J.; Wu, S.; Liu, Z.; Wu, K.; Fang, Z. Anionic polyacrylamide-assisted construction of thin 2D-2D WO_3/g-C_3N_4 Step-scheme heterojunction for enhanced tetracycline degradation under visible light irradiation. *J. Hazard. Mater.* **2020**, *393*, 122366. [CrossRef]
11. He, S.; Mo, Z.; Shuai, C.; Liu, W.; Yue, R.; Liu, G.; Pei, H.; Chen, Y.; Liu, N.; Guo, R. Pre-intercalation δ-MnO_2 Zinc-ion hybrid supercapacitor with high energy storage and Ultra-long cycle life. *Appl. Surf. Sci.* **2022**, *577*, 151904. [CrossRef]
12. Weng, B.; Liu, S.; Zhang, N.; Tang, Z.-R.; Xu, Y.-J. A simple yet efficient visible-light-driven CdS nanowires-carbon nanotube 1D–1D nanocomposite photocatalyst. *J. Catal.* **2014**, *309*, 146. [CrossRef]
13. Sun, M.W.; Shao, Y.; He, Y.; Zeng, Q.; Liang, H.; Yan, T.; Du, B. Fabrication of a novel Z-scheme g-C_3N_4/Bi_4O_7 heterojunction photocatalyst with enhanced visible light-driven activity toward organic pollutants. *J. Colloid Interface Sci.* **2017**, *501*, 123. [CrossRef]
14. Chen, D.; Wang, K.; Hong, W.; Zong, R.; Yao, W.; Zhu, Y. Visible light photoactivity enhancement via CuTCPP hybridized g-C_3N_4 nanocomposite. *Appl. Catal. B Environ.* **2015**, *166*, 366. [CrossRef]
15. Ma, D.; Wu, J.; Gao, M.; Xin, Y.; Chai, C. Enhanced debromination and degradation of 2,4-dibromophenol by an Z-scheme Bi_2MoO_6/CNTs/g-C_3N_4 visible light photocatalyst. *Chem. Eng. J.* **2017**, *316*, 461. [CrossRef]
16. Mei, S.; Gao, J.; Zhang, Y.; Yang, J.; Wu, Y.; Wang, X.; Zhao, R.; Zhai, X.; Hao, C.; Li, R.; et al. Enhanced visible light photocatalytic hydrogen evolution over porphyrin hybridized graphitic carbon nitride. *J. Colloid Interface Sci.* **2017**, *506*, 58. [CrossRef] [PubMed]
17. Zhu, M.; Li, Z.; Xiao, B.; Lu, Y.; Du, Y.; Yang, P.; Wang, X. Surfactant assistance in improvement of photocatalytic hydrogen production with the porphyrin noncovalently functionalized graphene nanocomposite. *ACS Appl. Mater. Interfaces* **2013**, *5*, 1732. [CrossRef] [PubMed]
18. Khusnutdinova, D.; Beiler, A.M.; Wadsworth, B.L.; Jacob, S.I.; Moore, G.F. Metalloporphyrin-modified semiconductors for solar fuel production. *Chem. Sci.* **2017**, *8*, 253. [CrossRef]

19. Li, X.; Liu, L.; Kang, S.-Z.; Mu, J.; Li, G. Differences between Zn-porphyrin-coupled titanate nanotubes with various anchoring modes: Thermostability, spectroscopic, photocatalytic and photoelectronic properties. *Appl. Surf. Sci.* **2011**, *257*, 5950. [CrossRef]
20. Gao, W.Y.; Chrzanowski, M.; Ma, S. Metal-metalloporphyrin frameworks: A resurging class of functional materials. *Chem. Soc. Rev.* **2014**, *43*, 5841. [CrossRef]
21. Kilian, K.; Pegier, M.; Pyrzynska, K. The fast method of Cu-porphyrin complex synthesis for potential use in positron emission tomography imaging. *Spectrochim. Acta A Mol. Biomol. Spectrosc.* **2016**, *159*, 123. [CrossRef] [PubMed]
22. Liu, S.; Zhou, S.; Hu, C.; Duan, M.; Song, M.; Huang, F.; Cai, J. Coupling graphitic carbon nitrides with tetracarboxyphenyl porphyrin molecules through π–π stacking for efficient photocatalysis. *J. Mater. Sci. Mater. Electron.* **2020**, *31*, 10677. [CrossRef]
23. Wang, J.; Zheng, Y.; Peng, T.; Zhang, J.; Li, R. Asymmetric Zinc Porphyrin Derivative-Sensitized Graphitic Carbon Nitride for Efficient Visible-Light-Driven H_2 Production. *ACS Sustain. Chem. Eng.* **2017**, *5*, 7549. [CrossRef]
24. Guo, F.; Li, L.; Shi, Y.; Shi, W.; Yang, X. Synthesis of N-deficient g-C_3N_4/epoxy composite coating for enhanced photocatalytic corrosion resistance and water purification. *J. Mater. Sci.* **2023**, *58*, 4223. [CrossRef]
25. Li, L.; Zhang, Y.; Shi, Y.; Guo, F.; Yang, X.; Shi, W. A hydrophobic high-crystalline g-C_3N_4/epoxy resin composite coating with excellent durability and stability for long-term corrosion resistance. *Mater. Today Commun.* **2023**, *35*, 105692. [CrossRef]
26. Lu, J.; Shi, Y.; Chen, Z.; Sun, X.; Yuan, H.; Guo, F.; Shi, W. Photothermal effect of carbon dots for boosted photothermal-assisted photocatalytic water/seawater splitting into hydrogen. *Chem. Eng. J.* **2023**, *453*, 139834. [CrossRef]
27. Shi, W.; Cao, L.; Shi, Y.; Chen, Z.; Cai, Y.; Guo, F.; Du, X. Environmentally friendly supermolecule self-assembly preparation of S-doped hollow porous tubular g-C_3N_4 for boosted photocatalytic H_2 production. *Ceram. Int.* **2023**, *49*, 11989. [CrossRef]
28. Shi, W.; Cao, L.; Shi, Y.; Zhong, W.; Chen, Z.; Wei, Y.; Guo, F.; Chen, L.; Du, X. Boosted built-in electric field and active sites based on Ni-doped heptazine/triazine crystalline carbon nitride for achieving high-efficient photocatalytic H_2 evolution. *J. Mol. Struct.* **2023**, *1280*, 135076. [CrossRef]
29. Shi, W.; Sun, W.; Liu, Y.; Zhang, K.; Sun, H.; Lin, X.; Hong, Y.; Guo, F. A self-sufficient photo-Fenton system with coupling in-situ production H_2O_2 of ultrathin porous g-C_3N_4 nanosheets and amorphous FeOOH quantum dots. *J. Hazard. Mater.* **2022**, *436*, 129141. [CrossRef]
30. Shi, Y.; Li, L.; Sun, H.; Xu, Z.; Cai, Y.; Shi, W.; Guo, F.; Du, X. Engineering ultrathin oxygen-doped g-C_3N_4 nanosheet for boosted photoredox catalytic activity based on a facile thermal gas-shocking exfoliation effect. *Sep. Purif. Technol.* **2022**, *292*, 121038. [CrossRef]
31. Shi, Y.; Li, L.; Xu, Z.; Guo, F.; Li, Y.; Shi, W. Synergistic coupling of piezoelectric and plasmonic effects regulates the Schottky barrier in Ag nanoparticles/ultrathin g-C_3N_4 nanosheets heterostructure to enhance the photocatalytic activity. *Appl. Surf. Sci.* **2023**, *616*, 156466. [CrossRef]
32. Sun, H.; Shi, Y.; Shi, W.; Guo, F. High-crystalline/amorphous g-C_3N_4 S-scheme homojunction for boosted photocatalytic H_2 production in water/simulated seawater: Interfacial charge transfer and mechanism insight. *Appl. Surf. Sci.* **2022**, *593*, 153281. [CrossRef]
33. Yuan, H.; Shi, W.; Lu, J.; Wang, J.; Shi, Y.; Guo, F.; Kang, Z. Dual-channels separated mechanism of photo-generated charges over semiconductor photocatalyst for hydrogen evolution: Interfacial charge transfer and transport dynamics insight. *Chem. Eng. J.* **2023**, *454*, 140442. [CrossRef]
34. Chen, T.; Zhong, L.; Yang, Z.; Mou, Z.; Liu, L.; Wang, Y.; Sun, J.; Lei, W. Enhanced Visible-light Photocatalytic Activity of g-C_3N_4/Nitrogen-doped Graphene Quantum Dots/TiO_2 Ternary Heterojunctions for Ciprofloxacin Degradation with Narrow Band Gap and High Charge Carrier Mobility. *Chem. Res. Chin. Univ.* **2020**, *36*, 1083. [CrossRef]
35. Pourhashem, S.; Duan, J.; Guan, F.; Wang, N.; Gao, Y.; Hou, B. New effects of TiO_2 nanotube/g-C_3N_4 hybrids on the corrosion protection performance of epoxy coatings. *J. Mol. Liq.* **2020**, *317*, 114214. [CrossRef]
36. Lin, L.; Hou, C.; Zhang, X.; Wang, Y.; Chen, Y.; He, T. Highly efficient visible-light driven photocatalytic reduction of CO_2 over g-C_3N_4 nanosheets/tetra(4-carboxyphenyl)porphyrin iron(III) chloride heterogeneous catalysts. *Appl. Catal. B Environ.* **2018**, *221*, 312. [CrossRef]
37. Zhu, K.; Zhang, M.; Feng, X.; Qin, L.; Kang, S.-Z.; Li, X. A novel copper-bridged graphitic carbon nitride/porphyrin nanocomposite with dramatically enhanced photocatalytic hydrogen generation. *Appl. Catal. B Environ.* **2020**, *268*, 118434. [CrossRef]
38. Wang, D.H.; Pan, J.N.; Li, H.H.; Liu, J.J.; Wang, Y.B.; Kang, L.T.; Yao, J.N. A pure organic heterostructure of μ-oxo dimeric iron(iii) porphyrin and graphitic-C_3N_4 for solar H_2 roduction from water. *J. Mater. Chem. A* **2016**, *4*, 290. [CrossRef]
39. Li, W.; He, X.; Ge, R.; Zhu, M.; Feng, L.; Li, Y. Cobalt porphyrin (CoTCPP) advanced visible light response of g-C_3N_4 nanosheets. *Sustain. Mater. Technol.* **2019**, *22*, e00114. [CrossRef]
40. Machado, G.S.; Wypych, F.; Nakagaki, S. Immobilization of anionic iron(III) porphyrins onto in situ obtained zinc oxide. *J. Colloid Interface Sci.* **2012**, *377*, 379. [CrossRef]
41. Jiang, G.; Yang, X.; Wu, Y.; Li, Z.; Han, Y.; Shen, X. A study of spherical TiO_2/g-C_3N_4 photocatalyst: Morphology, chemical composition and photocatalytic performance in visible light. *Mol. Catal.* **2017**, *432*, 232. [CrossRef]
42. Liu, C.; Raziq, F.; Li, Z.; Qu, Y.; Zada, A.; Jing, L. Synthesis of TiO_2/g-C_3N_4 nanocomposites with phosphate–oxygen functional bridges for improved photocatalytic activity. *Chin. J. Catal.* **2017**, *38*, 1072. [CrossRef]
43. Huang, C.; Lv, Y.; Zhou, Q.; Kang, S.; Li, X.; Mu, J. Visible photocatalytic activity and photoelectrochemical behavior of TiO_2 nanoparticles modified with metal porphyrins containing hydroxyl group. *Ceram. Int.* **2014**, *40*, 7093. [CrossRef]

44. Rezaeifard, A.; Jafarpour, M. The catalytic efficiency of Fe-porphyrins supported on multi-walled carbon nanotubes in the heterogeneous oxidation of hydrocarbons and sulfides in water. *Catal. Sci. Technol.* **2014**, *4*, 1960. [CrossRef]
45. Hao, R.; Wang, G.; Tang, H.; Sun, L.; Xu, C.; Han, D. Template-free preparation of macro/mesoporous g-C_3N_4/TiO_2 heterojunction photocatalysts with enhanced visible light photocatalytic activity. *Appl. Catal. B Environ.* **2016**, *187*, 47. [CrossRef]
46. Lv, B.; Lu, L.; Feng, X.; Wu, X.; Wang, X.; Zou, X.; Zhang, F. Efficient photocatalytic hydrogen production using an NH_4TiOF_3/TiO_2/g-C_3N_4 composite with a 3D camellia-like Z-scheme heterojunction structure. *Ceram. Int.* **2020**, *46*, 26689. [CrossRef]
47. Mousavi, M.; Soleimani, M.; Hamzehloo, M.; Badiei, A.; Ghasemi, J.B. Photocatalytic degradation of different pollutants by the novel gCN-NS/Black-TiO_2 heterojunction photocatalyst under visible light: Introducing a photodegradation model and optimization by response surface methodology (RSM). *Mater. Chem. Phys.* **2021**, *258*, 123912. [CrossRef]
48. Kong, L.; Ji, Y.; Dang, Z.; Yan, J.; Li, P.; Li, Y.; Liu, S.F. g-C_3N_4 Loading Black Phosphorus Quantum Dot for Efficient and Stable Photocatalytic H_2 Generation under Visible Light. *Adv. Funct. Mater.* **2018**, *28*, 1800668. [CrossRef]
49. Yang, S.; Gong, Y.; Zhang, J.; Zhan, L.; Ma, L.; Fang, Z.; Vajtai, R.; Wang, X.; Ajayan, P.M. Exfoliated graphitic carbon nitride nanosheets as efficient catalysts for hydrogen evolution under visible light. *Adv. Mater.* **2013**, *25*, 2452. [CrossRef]
50. Barrocas, B.T.; Ambrozova, N.; Koci, K. Photocatalytic Reduction of Carbon Dioxide on TiO_2 Heterojunction Photocatalysts—A Review. *Materials* **2022**, *15*, 967. [CrossRef]
51. Kumar, S.; Kumar, B.; Baruah, A.; Shanker, V. Synthesis of Magnetically Separable and Recyclable g-C_3N_4–Fe_3O_4 Hybrid Nanocomposites with Enhanced Photocatalytic Performance under Visible-Light Irradiation. *J. Phys. Chem. C* **2013**, *117*, 26135. [CrossRef]
52. Wei, M.; Wan, J.; Hu, Z.; Peng, Z.; Wang, B.; Wang, H. Preparation, characterization and visible-light-driven photocatalytic activity of a novel Fe(III) porphyrin-sensitized TiO_2 nanotube photocatalyst. *Appl. Surf. Sci.* **2017**, *391*, 267. [CrossRef]
53. Zhu, X.; Zhang, F.; Wang, M.; Ding, J.; Sun, S.; Bao, J.; Gao, C. Facile synthesis, structure and visible light photocatalytic activity of recyclable $ZnFe_2O_4$/TiO_2. *Appl. Surf. Sci.* **2014**, *319*, 83. [CrossRef]
54. Li, C.; Sun, Z.; Xue, Y.; Yao, G.; Zheng, S. A facile synthesis of g-C_3N_4/TiO_2 hybrid photocatalysts by sol–gel method and its enhanced photodegradation towards methylene blue under visible light. *Adv. Powder Technol.* **2016**, *27*, 330. [CrossRef]
55. Li, Y.; Lv, K.; Ho, W.; Dong, F.; Wu, X.; Xia, Y. Hybridization of rutile TiO_2 ($rTiO_2$) with g-C_3N_4 quantum dots (CN QDs): An efficient visible-light-driven Z-scheme hybridized photocatalyst. *Appl. Catal. B Environ.* **2017**, *202*, 611. [CrossRef]
56. Liu, C.; Dong, S.; Chen, Y. Enhancement of visible-light-driven photocatalytic activity of carbon plane/g-C_3N_4/TiO_2 nanocomposite by improving heterojunction contact. *Chem. Eng. J.* **2019**, *371*, 706. [CrossRef]
57. Hu, L.; Yan, J.; Wang, C.; Chai, B.; Li, J. Direct electrospinning method for the construction of Z-scheme TiO_2/g-C_3N_4/RGO ternary heterojunction photocatalysts with remarkably ameliorated photocatalytic performance. *Chin. J. Catal.* **2019**, *40*, 458. [CrossRef]
58. Wang, J.; Shi, W.; Liu, D.; Zhang, Z.; Zhu, Y.; Wang, D. Supramolecular organic nanofibers with highly efficient and stable visible light photooxidation performance. *Appl. Catal. B Environ.* **2017**, *202*, 289. [CrossRef]
59. Rabbani, M.; Heidari-Golafzani, M.; Rahimi, R. Synthesis of TCPP/$ZnFe_2O_4$@ZnO nanohollow sphere composite for degradation of methylene blue and 4-nitrophenol under visible light. *Mater. Chem. Phys.* **2016**, *179*, 35. [CrossRef]
60. Mahalakshmi, G.; Rajeswari, M.; Ponnarasi, P. Synthesis of few-layer g-C_3N_4 nanosheets-coated MoS_2/TiO_2 heterojunction photocatalysts for photo-degradation of methyl orange (MO) and 4-nitrophenol (4-NP) pollutants. *Inorg. Chem. Commun.* **2020**, *120*, 108146. [CrossRef]
61. Palanivel, B.; Lallimathi, M.; Arjunkumar, B.; Shkir, M.; Alshahrani, T.; Al-Namshah, K.S.; Hamdy, M.S.; Shanavas, S.; Venkatachalam, M.; Ramalingam, G. rGO supported g-C_3N_4/$CoFe_2O_4$ heterojunction: Visible-light-active photocatalyst for effective utilization of H_2O_2 to organic pollutant degradation and OH radicals production. *J. Environ. Chem. Eng.* **2021**, *9*, 104698. [CrossRef]
62. Abazari, R.; Mahjoub, A.R.; Salehi, G. Preparation of amine functionalized g-C_3N_4@(H/S)MOF NCs with visible light photocatalytic characteristic for 4-nitrophenol degradation from aqueous solution. *J. Hazard. Mater.* **2019**, *365*, 921. [CrossRef] [PubMed]
63. Palanivel, B.; Jayaraman, V.; Ayyappan, C.; Alagiri, M. Magnetic binary metal oxide intercalated g-C_3N_4: Energy band tuned p-n heterojunction towards Z-scheme photo-Fenton phenol reduction and mixed dye degradation. *J. Water Process Eng.* **2019**, *32*, 100968. [CrossRef]
64. Yi, F.; Gan, H.; Jin, H.; Zhao, W.; Zhang, K.; Jin, H.; Zhang, H.; Qian, Y.; Ma, J. Sulfur- and chlorine-co-doped g-C_3N_4 nanosheets with enhanced active species generation for boosting visible-light photodegradation activity. *Sep. Purif. Technol.* **2020**, *233*, 115997. [CrossRef]
65. Zarei, M.; Bahrami, J.; Zarei, M. Zirconia nanoparticle-modified graphitic carbon nitride nanosheets for effective photocatalytic degradation of 4-nitrophenol in water. *Appl. Water Sci.* **2019**, *9*, 175. [CrossRef]
66. Ma, L.; Wang, G.; Jiang, C.; Bao, H.; Xu, Q. Synthesis of core-shell TiO_2@g-C_3N_4 hollow microspheres for efficient photocatalytic degradation of rhodamine B under visible light. *Appl. Surf. Sci.* **2018**, *430*, 263. [CrossRef]
67. Huang, K.; Li, C.; Zhang, X.; Meng, X.; Wang, L.; Wang, W.; Li, Z. TiO_2 nanorod arrays decorated by nitrogen-doped carbon and g-C_3N_4 with enhanced photoelectrocatalytic activity. *Appl. Surf. Sci.* **2020**, *518*, 146219. [CrossRef]

68. Zhang, X.; Li, L.; Zeng, Y.; Liu, F.; Yuan, J.; Li, X.; Yu, Y.; Zhu, X.; Xiong, Z.; Yu, H.; et al. TiO_2/Graphitic Carbon Nitride Nanosheets for the Photocatalytic Degradation of Rhodamine B under Simulated Sunlight. *ACS Appl. Nano Mater.* **2019**, *2*, 7255. [CrossRef]
69. Huang, Y.; Wang, W.; Zhang, Q.; Cao, J.J.; Huang, R.J.; Ho, W.; Lee, S.C. In situ Fabrication of alpha-Bi_2O_3/$(BiO)_2CO_3$ Nanoplate Heterojunctions with Tunable Optical Property and Photocatalytic Activity. *Sci. Rep.* **2016**, *6*, 23435. [CrossRef] [PubMed]
70. Chen, Y.; Huang, W.; He, D.; Situ, Y.; Huang, H. Construction of heterostructured g-C_3N_4/Ag/TiO_2 microspheres with enhanced photocatalysis performance under visible-light irradiation. *ACS Appl. Mater. Interfaces* **2014**, *6*, 14405. [CrossRef]
71. Barrocas, B.; Chiavassa, L.D.; Conceicao Oliveira, M.; Monteiro, O.C. Impact of Fe, Mn co-doping in titanate nanowires photocatalytic performance for emergent organic pollutants removal. *Chemosphere* **2020**, *250*, 126240. [CrossRef] [PubMed]
72. Barrocas, B.T.; Osawa, R.; Oliveira, M.C.; Monteiro, O.C. Enhancing Removal of Pollutants by Combining Photocatalysis and Photo-Fenton Using Co, Fe-Doped Titanate Nanowires. *Materials* **2023**, *16*, 2051. [CrossRef] [PubMed]
73. Adler, A.D.; Longo, F.R.; Finarelli, J.D.; Goldmacher, J.; Assour, J.; Korsakoff, L. A simplified synthesis for meso-tetraphenylporphine. *J. Org. Chem.* **1967**, *32*, 476. [CrossRef]